An advanced analytical assessment of rare earth element concentration, distribution, speciation, crystallography and solid-state chemistry in fly ash

Ilemona C. Okeme [a]*, Peter G. Martin [a], Christopher Jones[a], Richard A. Crane [b], Theophilus I. Ojonimi [c], Konstantin Ignatyev [d], Thomas B. Scott [a]

[a] Interface Analysis Centre, School of Physics, University of Bristol, HH Wills Physics Laboratory, Bristol, BS8 1TL, United Kingdom.

[b] Camborne School of Mines, College of Engineering, Mathematics and Physical Sciences, University of Exeter, UK; Environment and Sustainability Institute, University of Exeter, UK.

[c] Department of Mining Engineering, University of Jos, Jos, 930222, Nigeria.

[d] Diamond Light Source Limited, Harwell Science and Innovation Campus, Didcot, Oxfordshire.

*** Corresponding author**:

Email: io17820@bristol.ac.uk

Tel: +44 (0) 117 33 17686

Highlights

- The total rare earth content of the studied samples is promising for recovery.
- Critical rare earths comprised 30wt% of rare earth content within samples studied.
- Micromanipulation method employed to isolate individual monazite particles.
- Radial zonation observed in monazite particles, with rim rich in rare earths.
- Ce oxidised and monazite structure amorphized, increasing chemical reactivity.

Abstract

Fly ash represents a promising alternative source of rare earth elements (REE). However, information on REE containing mineral phases and their association with other fly ash components, vital for REE recovery from fly ash, is currently lacking. Herein, the mass fraction, distribution, crystallography and solid-state chemistry of REE, U and Th in Nigerian simulated fly ash samples were characterised using a range of laboratory and synchrotron x-ray based analytical techniques to underpin future extraction methodologies. Inductively coupled plasma mass spectrometry following full-acid digest of forty-five samples revealed recoverable average total REE content which ranged between 442 $mgkg^{-1}$ and 625 $mgkg^{-1}$, comprising over 30wt% of the critical REE Nd, Eu, Tb, Dy, Y and Er. These REE within the fly ash samples were found to be most frequently associated with discrete monazite, xenotime and Y-bearing zircon mineral particles, with the former the most detected, which could be beneficiated through gravity separation. Analysis of monazite particles isolated from the composite samples through a complimentary suite of analytical synchrotron radiation techniques revealed a core-shell pattern, with the shell rich in colocalised Ce, Nd and La, and the core enrich in both U and Th. Ce in monazite was found to exist in a mixed trivalent and tetravalent oxidation state, with the monazite structure amorphized due to the high temperature combustion process. Such results demonstrate the strong co-association and physical distribution of REE, U and Th within monazite in fly ash; knowledge of which can subsequently be used to optimise or develop a more selective, cost-effective and environmentally friendly solvent extraction methodology, by targeting the strongly colocalised and surface bound REE in fly ash monazite particles.

Keywords: Nigeria; fly ash; rare earth elements; monazite; synchrotron radiation.

1. Introduction

Owing to their unique chemical and physical properties, the rare earth elements (REE) are of fundamental industrial importance, with applications including automobiles, green energy, electronics and defence [1,2]. REE consist of chemically similar elements; the fourteen naturally occurring

lanthanides, plus Y and Sc [3]. Based on their electronic configuration, these elements are further subdivided into the light rare earth elements (LREE) (La to Gd) and the heavy rare earth elements (HREE) (Tb to Lu with Sc and Y) [4]. REE rarely occur in easily exploitable high-grade deposits and never occur as native metals. Their use in final products is therefore dependent upon their efficient extraction from their host minerals [5,6]. When compared against their total average crustal abundance (typically 160 $mgkg^{-1}$ to 205 $mgkg^{-1}$ [7]), their mass fraction within minerals and ores is relatively low [3]. Out of the approximately 200 minerals known to contain significant quantities of REE, only bastnaesite ([Ce, La]CO_3F), monazite ([Ce,La,Nd,Th]PO_4), xenotime (YPO_4) and ion-adsorption clays are mined commercially for REE production; with monazite and bastnaesite typically exploited for LREE minerals, and xenotime and ion-adsorption clays for the HREE [8,9]. These REE minerals are accessory minerals of U and Th and are therefore invariably radioactive, constituting a commensurate human health and environmental hazard [9].

Currently, more than 75% of REE production, nearly half of the known reserves, and the majority of REE metallurgical technologies occur (or are located) in China [2]. Resulting from this near total market monopoly coupled with recent instabilities in the global REE supply market and the projected explosion in demand over the coming decades [2], there is now a renewed incentive for countries to secure economically sustainable REE supply. Amongst this there are a growing number "unconventional sources" such as coal and coal waste products (e.g. coal mine waste, fly ash, acid mine drainage and mine tailings) which have emerged in recent years as highly viable targets for REE recovery [8].

With billions of tons of fly ash already stored in repositories globally, and millions produced annually (especially in the USA, China and India), the development of new methodologies to extract REE from this major untapped resource is urgently required. Following changes in USA-China trading activity in recent years, the USA Senate reintroduced the REE Advanced Coal Technologies Act (REEACT),

initiating research into the development of technologies capable of extracting REEs from coal and coal by-products [10].

The recovery of REEs from fly ash rather than coal and traditional REE-containing ores has several notable advantages [8]. It is a cheap and readily-available post-combustion by-product enriched in inorganic REE minerals such as phosphates, by a factor of six to ten relative to precursor coal depending on the geological origin of the feedstock (a consequence of their high melting, boiling, and thermal decomposition temperatures) [11,12]. Furthermore, fly ash does not require extensive excavation, unlike the mining of REE ores, which represents a significant capital investment and is environmentally destructive - REE mining process generates large volumes of waste rock that is rich in radionuclides. In addition, coal fly ash is an inorganic fine powder, therefore making it ideal for chemical processing by eliminating the need for costly and energy intensive crushing and grinding.

Previous studies have demonstrated the occurrence and distribution of REE in coal deposits and their respective ash by-products deposits [13,14]. Seredin et al [14], used inductively coupled plasma-mass spectrometer (ICP-MS) to characterise coal samples from Russia's Pavlovka coal deposit and found the REE concentration to be up to 1290 $mgkg^{-1}$, with the REE in the resulting ash having a mass fraction (wt%) of 1%. Two further ICP-MS studies of ash samples from a power plant burning coal from the Kentucky Fire Clay coal bed (a lithology rich in volcanic ash) observed a REE contents of 1200 $mgkg^{-1}$ to 1670 $mgkg^{-1}$ [11,12]. Recent surveys published by the United States Department of Energy (US DoE) indicated total REE contents (not including Sc) of 41 $mgkg^{-1}$ to 1286 $mgkg^{-1}$ in U.S. fly ash [15,16]. Additional studies on fly ash using scanning electron microscopy (SEM) coupled with energy dispersive (x-ray) spectroscopy (EDS), has shown the main REE-bearing phases retained in fly ash to be phosphate minerals (monazite and xenotime), zircon ($ZrSiO_4$), bastnaesite, Ce-Nd bearing carbonates, and organically associated lanthanides [17-19].

Synchrotron techniques such as micro-x-ray fluorescence (μ-XRF) and micro-x-ray absorption near edge structure (μ-XANES) have been used extensively to characterise trace metal distribution and

speciation in different geological materials [20,21]. Within this there have been several studies where the Ce L_{III} absorption edge in geological materials has been investigated [22,23]. However, while synchrotron radiation techniques (such as μ-XRF and μ-XANES) have formerly been utilised to examine the REE composition and distribution within fly ash samples [24,25], other synchrotron radiation techniques such as μ-XRF tomography and micro-x-ray diffraction (μ-XRD) have not been exploited. Therefore, studies employing such enhanced synchrotron radiation techniques represent a powerful means to derive unique information on REEs; such as an elements oxidation state (at the micron scale), speciation, distribution within REE minerals and alterations to the crystallographic structure, for combined elucidation of geochemical and thermal changes in the REE minerals within the residual fly ash following the combustion of the precursor coal.

This study has been established to characterise REE-bearing minerals contained within Nigerian fly ash samples. To meet this end, single REE-bearing particles within bulk fly ash samples were extracted from the surrounding matrix prior to synchrotron analysis (μ-XRF and μ-XANES). μ-XRD and μ-XRF tomography characterisation of such minerals was performed to obtain further insight (through 2D and 3D models) into the structural transformation that may occur as a result of the combustion processes, and the REEs distribution pattern within individual monazite micro particles. The results obtained are essential in developing a fundamental understanding of the distribution and colocalisation of REE, U and Th within monazite particles, and therefore in the optimisation of recovery methods for such metals/minerals for both resource recovery and environmental protection [26].

2. Materials and Methods

2.1 Study Area

The study examines material sourced from three open-pit coal mines located in Kogi state, Nigeria, as shown in Figure 1 [27]: both Okaba (OKA) and Odagbo (ODA) mines are located in Okaba and Odagbo, respectively, within the Ankpa Local Government Area (LGA), with Omelewu (OMA) coal mine located in Imane, within the Olamaboro LGA. The coal mines host sub-bituminous coal (part of the Mamu

Formation) and belong to the Kogi mining district, comprising an area of 225 thousand hectare [28,29]. Further information on the geologic setting and the coal from these coal mines can be found in [28-32]. Currently, these coal deposits are commercially mined for coal briquette production and as an energy source for nearby cement production [33,34]. Nigeria has known coal reserves of approximately 639 million metric tonnes, with additional estimated reserves of approximately 2750 million metric tonnes [35].

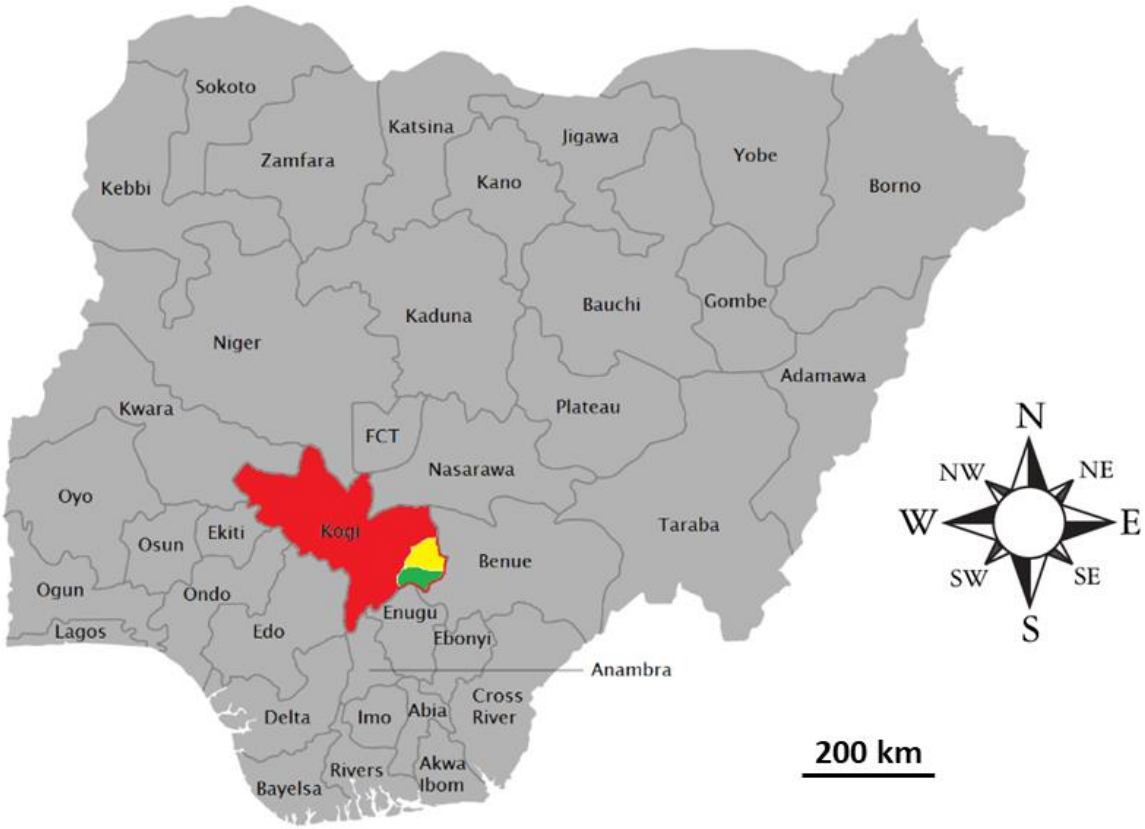

Figure 1: Map of Nigerian states showing the location of Ankpa LGA (yellow), and Olamaboro LGA (green) both in Kogi state (red). Modified from [27].

2.2 Samples Collection and Preparation

Coal samples (each approximately 200 g, packed in polythene bags) were collected from across the three mines using a stratified random sampling method to obtain representative material.

Since Nigeria's coal-fired power plants are only at an advanced stage of planning (that is, no operational coal-fired power plants exist in Nigeria from which to obtain fly ash samples), simulant fly

ash samples were studied in this work. To simulate fly ash within the laboratory, crushed samples were oven-dried at 100°C for 30 minutes, then pulverised and homogenised before being passed through a 150 µm mesh sieve. The samples were then combusted using a muffle furnace at 1100°C (below the fusion temperature of the ash, while completely removing the organic matter content). This selection of combustion temperature also approximates to the temperature used in coal-fired power plants burning low rank coal (Lignite and sub-bituminous) [36]. The implication of burning low rank coal (at a low temperature) over high rank coal is that it is more likely for the rare earth mineral particles to exist as discretely rather than being encapsulated in the glassy component of ash, since the melting temperatures of glass forming aluminosilicate minerals are higher than this combustion temperature. Following ashing, the samples were left to cool. Sieve analysis revealed that about 80% of these coal ash materials fell in the particle size range of 1 to 300 µm, which translated to 80% fly ash and 20% bottom ash.

2.3 Elemental composition and mineralogical analysis

2.3.1 XRF and XRD analysis

To determine the major elements (as oxide ratios) and trace heavy toxic metals in the bulk fly ash samples, a total of 15 fly ash samples per coal mine were analysed using a benchtop Niton™ FXL 950 XRF analyser (Ag anode with 50 kV/80 µA maximum X-ray tube, and Si-PIN semiconductor detector). The Niton™ FXL 950 XRF analyser is self-calibrating – running on a factory installed calibration software (called 'Fundamental Parameter' (FP)), to accurately measure elemental concentrations and automatically correct for matrix and inter-element effects. Prior to samples analysis, the calibration of the analyser was further checked and confirmed not to have drifted by running two reference materials (USGS SdAR-M2 and NIST 2709a). The pulverised, homogenised and sieved fly ash samples (Section 2.2) were each packaged into XRF sample cups and scanned for two (2) minutes (live time); to ensure an accurate reading and increased sensitivity. Normalisation and quantification of the results were performed using the Thermo Scientific Inc. NDT™ package.

Mineralogical analysis of the fly ash samples was performed on composite OMA, OKA and ODA bulk fly ash samples using a Philips X'pert™ diffractometer system with a Cu anode operated at a voltage and current of 40 kV and 30 mA, respectively. The scans were run from 10 to 80 degrees 2θ, with increments of 0.07 degrees at a counting time of 10 seconds per step. The minerals phases were then determined and quantified using the match™ phase identification package.

2.3.2 ICP-MS analysis of REE

The REE mass fraction of each fly ash sample was analysed using total acid digestion followed by ICP-MS using the method of Garbe-Schönberg [37]. A total of 45 fly ash samples (15 per coal mine) were prepared for analysis. The samples were first homogenised by gentle agitation and 100 mg was transferred into individual 50 mL screw cap teflon digestion vessels. 4mL of HF (47-51% Trace metal grade; Fisher Scientific) followed by 3 mL of HCl (34-37% Trace metal grade; Fisher Scientific) and then 1 mL of HNO_3 (67-69% Trace metal grade; Fisher Scientific) was then added to each sample using a micropipette. Time was allowed between each step to allow any reactions to subside. The reaction vessels were then sealed, and each placed in DigiPrep digestion blocks (preheated to 160°C) for 18 hours. The vessels were then removed from the DigiPrep system and allowed to cool to room temperature. 1 mL of $HClO_4$ (65% Normatom; VWR™) was then added to each sample which were then returned to the DigiPrep system and heated to 180°C until incipient dryness.

Samples were then removed from the DigiPrep system and allowed to cool to room temperature. This step was then repeated but using 1 mL HNO_3 (67-69% Trace metal grade; Fisher Scientific). 1 mL of conc. HNO_3 (67-69% Trace metal grade; Fisher Scientific) and 5 mL of deionised water were then added to each sample which were returned to the DigiPrep system and heated to 100°C for 30 minutes. Samples were then removed from the DigiPrep system and allowed to cool to room temperature. 44 mL of deionised water were then added to each sample.

Samples were then prepared for ICP-MS analysis by diluting 5 mL aliquots using 45 mL of 5% HNO_3. (67-69% Trace metal grade; Fisher Scientific). Measurements was performed using an Agilent 7700x. Duplicates, blanks and replicates of a Reference Material (USGS: AGV-1 and DNC-1) were ran for every 10 samples. Calibration was performed using a Inorganic ventures ICP-71A multi-elemental ICP-MS calibration standard.

2.4 SEM-EDS REE Particle Location

Representative composite OMA, OKA and ODA bulk ash samples for initial analysis within the SEM were prepared by depositing a fine layer of fly ash (<1 g) on to a 12 mm low elemental background adhesive carbon (Leit) disc mounted on a standard SEM pin-stub. The samples were then examined using a Zeiss SIGMA™ Field Emission SEM fitted with secondary electron (Everhart Thornley SE2) and backscattered electron (AsB) detectors using the instrument's Variable Pressure (VP) mode to negate against the requirement for a conductive coating while preventing surface charging. Using the backscattered electron detector (AsB), mineral particles containing trace levels of high atomic (Z) number elements in the samples (e.g. REE minerals) appeared as bright (white) spots against the otherwise dark sample background. REE mineral particles were then identified based on their characteristic elemental composition following confirmatory EDS analysis. The elemental composition and subsequently the mass fraction (wt% ± percentage error, δ) were determined using an EDAX™ Octane Plus high-resolution EDS system comprising an electronically cooled Silicon Drift Detector (SDD). At a voltage of 30 keV, aperture of 120 µm (in high current mode) and acquisition time of 200 second, the whole surface of each identified REE mineral particle was raster scanned, and data analysis undertaken using the associated EDAX (AMETEK Inc.) TEAM™ software.

2.5 REE Particle Isolation

Following the particles prior identification, in-situ removal of the identified micron-scale REE-bearing monazite particles from the bulk samples was performed within the SEM using an MM3A-EM Micromanipulator from Kleindiek Nanotechnik [38]. This piezo-electric device, capable of stepwise

vertical, retractive, rotational and lateral motion at minimum incremental movements of 1 nm was used to control an extruded glass capillary with a tip diameter of approximately 1 µm. To negate against the effects of electron beam induced charging, the non-conductive extruded glass capillary was coated with approximately 2 nm of sputter-deposited gold.

The lift-out process reported in Martin et al [39] for uranium particles was used in this work to extract the REE containing monazite particles – similarly utilising the electron-beam hardening adhesive SEMGlu™, also by Kleindiek [40]. A schematic of the isolation process is detailed in Figure 2. Following their SEM-EDS characterisation, each monazite particle extracted from the bulk fly ash (still adhered to the glass capillary needle) was securely enclosed in Kapton™ tape in preparation for subsequent synchrotron radiation analysis. Owing to the morphological and compositional similarities of the suite of monazite particles identified in the composite OKA, ODA and OMA fly ash samples, only three (3) monazite particles were prepared in this way for synchrotron analysis.

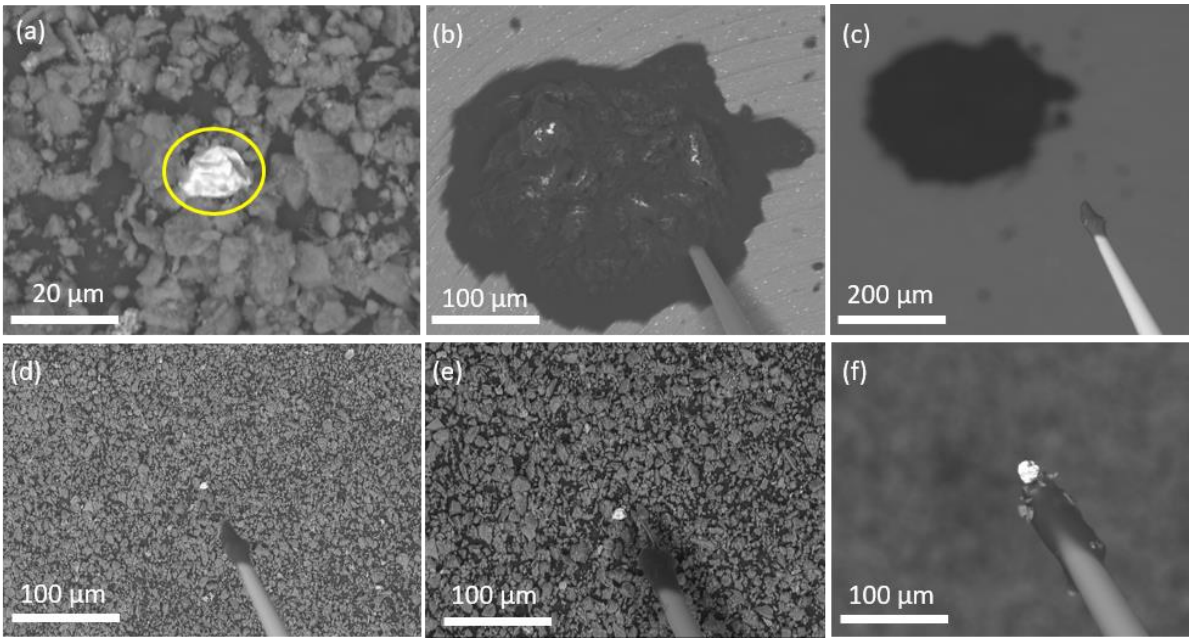

Figure 2: In-situ REE particle isolation process performed within the Zeiss SIGMA VP SEM using the Kleindiek MM3A Micromanipulator. (a) locating particle using backscattered electron detector and co-incident EDS; (b) and (c) applying small quantity of the electron-beam hardening SEMGlu™ to the extruded tip of glass capillary; (d) and (e) progressively lowering the glass capillary to approach the particle (f) removing the particle from the surrounding bulk material, attached to the capillary tip.

2.6 Synchrotron Radiation Analysis

Synchrotron μ-XRF, μ-XRF tomography, μ-XANES and μ-XRD analyses were performed at Diamond Light Source on the micro-focus spectroscopy beamline (I18). Diamond is a medium-energy third generation synchrotron with the storage ring operated at 3 GeV and nominal beam current of 300 mA. The I18 beamline, with an energy range of 2.05 keV and 20.5 keV, is equipped with a cryogenically cooled double crystal Si[111] monochromator (for energy tuning) and Kirkpatrick–Baez (KB) mirrors for the focusing of the beam (to a spot of 2 μm × 2 μm) onto the sample, and harmonic rejection. The beamline was equiped with a Vortex-ME4™ multi-element Silicon drift fluorescence detector (SDD) and a high-resolution X-ray scientific Complementary Metal–Oxide–Semiconductor (sCMOS) camera for μ-XRF, μ-XRF tomography, μ-XANES and μ-XRD data acquisition, respectively. To prevent detector saturation, a 0.1 mm Al foil was inserted. Further details of the optical and detector setup of the I18 beamline can be found in Mosselmans et al [41]. Throughout all sample analyses, a consistent beam, sample and detector geometry were maintained.

2.6.1 μ-XRF

Each particle was mounted on a kinematic stage at 45° to the incident beam, with the fluorescence detector oriented at 90° (perpendicular) to the incident beam. Each particle was raster-scanned through the beam at an energy of 18 keV (above the L_{III} edge energies of Ce (5723 eV), Nd (6208 eV), La (5483 eV), U (17166 eV) and Th (16300 eV)) using a step size of 2.5 μm, and dwell-time of 30 second per step. Resulting from the comparably thin sample thickness, elemental composition data was acquired in fluorescence mode using the Vortex-ME4™ multi-element Silicon drift fluorescence detector (SDD) – fitted using PyMCa and visualised in 2D using Diamond's in-house DAWN software [42].

2.6.2 µ-XRF tomography

The µ-XRF technique provides a depth averaged 2D representation of a 3D distribution of elements, hence does not reveal 3D information on the location of elements on the surface or within a particle. This limitation is resolved through µ-XRF tomography technique**.** µ-XRF tomography analysis was performed on monazite particle **A**, to obtain 3D information on REE, U and Th distribution in the particle. For each fluorescence tomographic scan, the particle was raster scanned while progressively being translated through the beam (using a step size of 2.5 µm), and then rotated through 180° with constant angular steps of 3°, at a dwell-time of 60 millisecond. Fluorescence projections were acquired using a sCMOS x-ray camera coupled with a gadolinium oxysulphide scintillator screen. Corrections for absorption within the particle matrix and reconstruction of the fluorescence projections collected was completed using iterative algorithms, with a 3D volumetric rendering of the particle performed using the FEI Avizo™ software [43].

2.6.3 µ-XANES

Following the µ-XRF analyses, µ-XANES data were acquired (at respective L_{III} edge energy) for Ce (5723 eV), Nd (6208 eV) and La (5483 eV) at spots identified as containing high concentrations of these elements within each monazite particle. For each of Ce, La and Nd, in the pre and post edge regions, energy steps of 0.25 eV were used, with steps of 0.1 eV used across the main edge region using a dwell-time of 30 seconds per step. µ-XANES data were processed (calibrated against respective Ce, La and Nd L_{III} edge energies, deglitched, normalised and fitted) using the ATHENA software suite [44]. The quantification of Ce (III) and Ce (IV) in the normalised µ(E) Ce µ-XANES spectrum was undertaken in ATHENA by linear combination fitting (LCF), using a fit range of -30 eV to 70 eV around the Ce L_{III} edge. The weights of the reference compounds were forced to be between 0 and 1 with no restriction on the edge energy, E_0.

2.6.4 μ-XRD

For μ-XRD, the sCMOS camera was aligned directly downstream of the sample along the path of the beam of energy, 18 keV. The sample was rotated through 180° during exposure and data acquired in transmission mode. Data processing (background correction, 2D and 1D visualisations) of the diffraction patterns were additionally performed using the DAWN software.

3. Results and Discussion

3.1 XRF and XRD analysis

Table S1 (Appendix) and Figs. S1, S2, and S3 (Appendix) show the XRF and XRD results for OMA, OKA and ODA fly ash samples. The average XRF results (in wt%) showed that the fly ash samples are largely composed of SiO_2 (>54%) and Al_2O_3 (>19%), alongside 2% to 7% Fe_2O_3, TiO_2 and CaO (except for OMA samples with CaO level of less than 1%). In OMA, OKA and ODA samples, the sum of SiO_2, Al_2O_3 and Fe_2O_3 were greater than 70% with CaO level also less than 8%; this implies OMA, OKA and ODA fly ash classify as class F according to the ASTM standard [45]. Previous study has shown that high calcium concentration (as in the case of OKA and ODA) is associated with extractability of REE associated with calcium-bearing phases in the fly ash, due to the high solubility of the calcium-bearing phases in nitric acid [46]. Results from previous proximate analysis carried out on OMA, OKA and ODA fly ash samples by Afu et al., Mohammed et al. and Chukwu et al. [30-32] (table S2 (Appendix)) shows that OMA, OKA and ODA fly ash have ash content (in wt%) of 14.8%, 10.7% and 5.3%, respectively. This result agrees with studies on fly ash sourced from coal-fired power plants [24,47]. Although occurring as few to hundreds of $mgkg^{-1}$ relative to the large volume of fly ash that would be generated annually, the trace toxic heavy metals (Pb, As, and Cr) are of serious environmental concern and capital intensive during rare earth extraction.

The results (in wt%) from XRD analysis showed quartz (SiO_2) and mullite ($3Al_2O_3.2SiO_2$) as the major mineral phase alongside trace amount (of less than 1%) of hematite and cristobalite (polymorph of

quartz formed during the high temperature combustion process). These results also agree with the XRD studies on fly ash samples from coal-fired power plants [15,47].

3.2 ICP-MS analysis of REE and economic valuation

Shown in Tables S3, S4 and S5 (Appendix), respectively, are the complete results of REE measurement with ICP-MS for OMA, OKA and ODA fly ash samples. The samples were highly concentrated in the LREE, with Ce followed by Nd the most abundant LREE in all samples. Of the HREE, Y, Sc, Gd and Dy were the most abundant, with Eu, Tb, Ho, Tm and Lu being just a few $mgkg^{-1}$ (characteristic of non-ore HREE sources), indicating low occurrence of HREE minerals in the studied fly ash samples. This abundance pattern of the light and the heavy REE in the fly ash samples conforms to the Oddo-Harkins Rule, where in this case, the REE with even atomic number (Z) are more abundant than the ones with odd Z.

As shown in Table 1, the mean total REE (plus Y and Sc) for OMA, OKA and ODA were 623 $mgkg^{-1}$, 442 $mgkg^{-1}$ and 441 $mgkg^{-1}$ respectively, with the fraction of the critical REE (Nd, Eu, Tb, Dy, Y and Er) being 37%, 30% and 28%, respectively. When compared with the Upper Continental Crust Abundance (UCCA) as in Tables S3, S4 and S5 (Appendix), the total REE content were 2 to 4 times enriched in the fly ash samples (with Ce being 6 times enriched in the OMA fly ash). Though these concentrations were generally well below concentrations in conventional REE ores [3], the large volume fly ash generated annually in addition to little or no extra cost of ore mining and waste rock handling is a significant advantage. These results are comparable with results of previous studies on USA, Chinese and Indian fly ash samples (Table 1).

Table 1: Comparison of mass concentration ($mgkg^{-1}$) of total REE (TREE) in fly ash with those of top coal consuming countries.

Coal source	TREE	Critical REE (%)	Reference
Omelewu coal, Nigeria	623	37	This study
Okaba coal, Nigeria	442	30	This study
Odagbo coal, Nigeria	441	28	This study
Jungar, Inner Mongolia, China	293.5	28.3	Dai et al., 2014b [48]
Bhusawal coal plant (unspecified mine), India	384.1	26.3	Modal et al., 2019 [49]
Central Appalachian (Fire Clay), USA	1667.6	36.5	Mardon and Hower, 2004 [50]
Central Appalachian, USA	401.5	38.6	Hower et al., 2013b [51]
Illinois Basin, USA	312.1	36.2	Hower et al., 2013b [51]
Central Appalachian, USA	563.6	38.1	Hower et al., 2013b [51]
Powder River Basin, USA	283.2	32.8	Taggart et al., 2016 [52]

3.2.1 Economic valuation of REE content of fly ash

Table S6 (Appendix) shows the REE mass fractions expressed as rare earth oxide (REO), with OMA REO mean value slightly higher than that of Round Top Mountain-a rhyolite laccolith intrusion enriched in Y and other HREE [53]. On REO basis, the economic valuation shows that these fly ash samples have very strong potential of recovering REO worth millions of dollars. Using the ash content values of OMA, OKA and ODA fly ash samples (14.8%, 10.7% and 5.3%, respectively), (Table S2 (Appendix)), and an initial projected annual consumption of 27 million metric tonnes of coal by the proposed coal-plants [28], this amounts to 1330 thousand, 960 thousand and 480 thousand metric tonnes of fly ash generated annually from OMA, OKA and ODA coal mines, respectively (assuming equal supply of coal

from all mines). Using the REO values (Table S6 (Appendix)), we estimated that a total of 1752 tonnes/year (1 751 844.7 kg/year) of REO is recoverable from Nigerian fly ash, translating into annual value of $41 204 000 dollars (Table S7 (Appendix)). Though this economic valuation does not include costs of recovery (with cost-effective technologies currently under development), it provides the basis for evaluating viability of REE extraction from fly ash. One major advantage of using fly ash as alternative source of REE is the minimal expense associated with the mining processes, such as blasting, prospecting, and transport. The measurement results also show that the potential value of REE in fly ash is dependent on REE class (LREE vs HREE), with the high prices of Sc, Nd and the HREE, contributing considerably to the REE value in fly ash.

3.3 SEM-EDS

Fig. 3a is an SEM image showing the distribution and abundance of REE minerals in a fly ash sample. Fig. 3b shows the SEM image and EDS spectra of three monazite particles **A**, **B** and **C**, respectively. Also, the mass fraction (wt% ± percentage error, δ) elemental composition of ten (10) monazite particles identified within composite OMA, OKA and ODA samples, respectively, is shown in Table S8 (Appendix). These are typical of the suite of monazite particles found in the fly ash samples studied. From the SEM-EDS results, trace monazite particles were the predominant REE mineral within the fly ash samples, alongside scanty xenotime and Y-bearing zircon particles (Figs. S4a and S4b (Appendix) and Table S9 (Appendix)). This confirms the ICP-MS result which recorded highest concentration for Ce and Y. As can be seen in Fig. 3b and table S8 (Appendix), the detected monazite particles were the same in composition and morphology, with weathered surfaces characteristic of monazite of detrital origin. Strong Al and Si peaks signified the occurrence of quartz and mullite, the major mineral phases in fly ash [24]. The monazite particles are ascribed to a detrital source, transported by water or wind from a nearby granitic highland, deposited and subsequently incorporated into the coal during coalification [18]. These REE minerals (between 10 µm and 80 µm in size) were found to exist largely as discrete particles and not encapsulated in glassy phases, making the extraction and isolation of

these discrete particles more cost-effective, as leaching rare earth mineral particles encapsulated in glassy phases consumes more costly reagents and generates significant volumes of waste products. Y though abundant in the fly ash materials, its extraction will be difficult since its host mineral (zircon) is a refractory mineral. Studies have shown that REE mineral particles become encapsulated in quartz and mullite mineral particles during coal combustion process, mainly during the combustion of high rank coal at temperatures between 1500°C and 1700°C) [46,47]. Hence, combustion of low rank coal at temperatures between 900°C and 1200°C greatly reduces sequestration of REE minerals into aluminosilicate glass phases, making REE extraction from fly ash cost effective. Our results agreed with previous studies on fly ash (sourced from coal-fired plants burning high rank coal) that REE mineral particles were either dispersed throughout the glass phase, or as independent particles outside of glass [17].

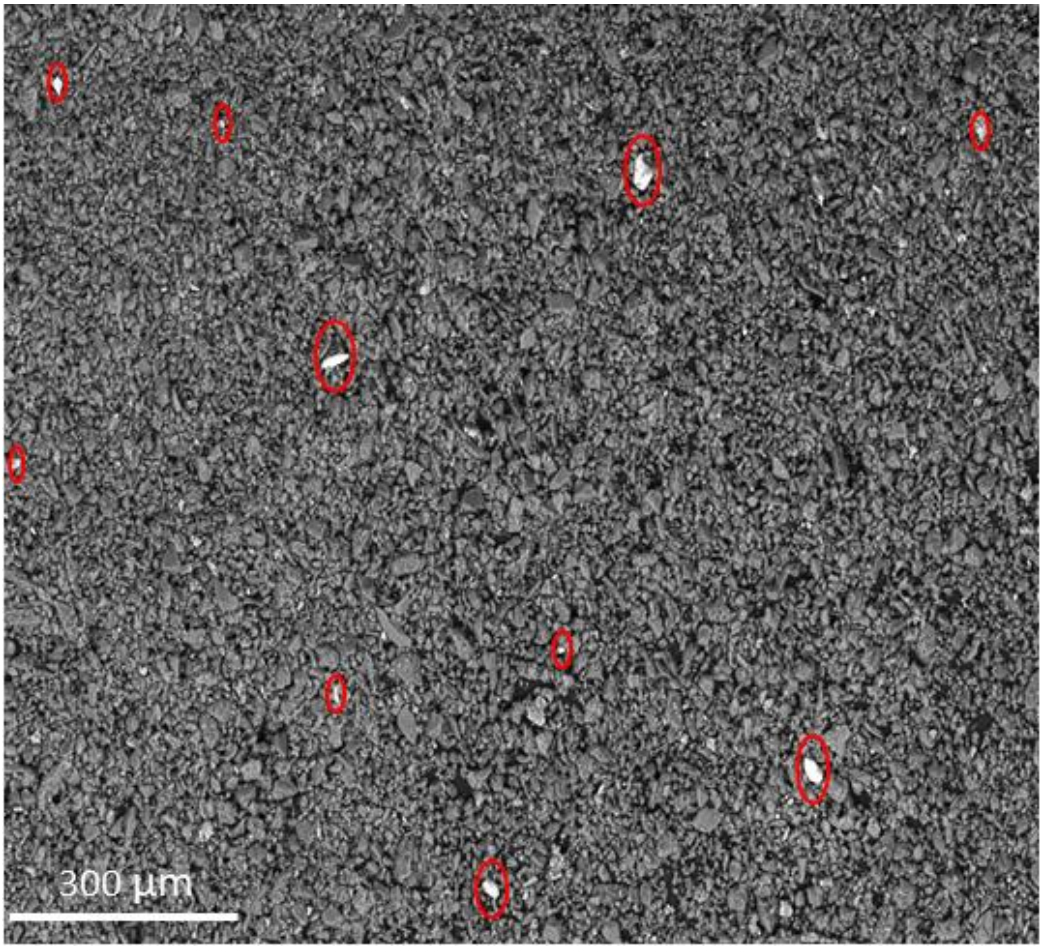

Fig. 3a: Backscattered electrons image showing distribution and abundance of micro REE mineral particles in a fly ash sample, with the particles appearing white in contrast to the surrounding material.

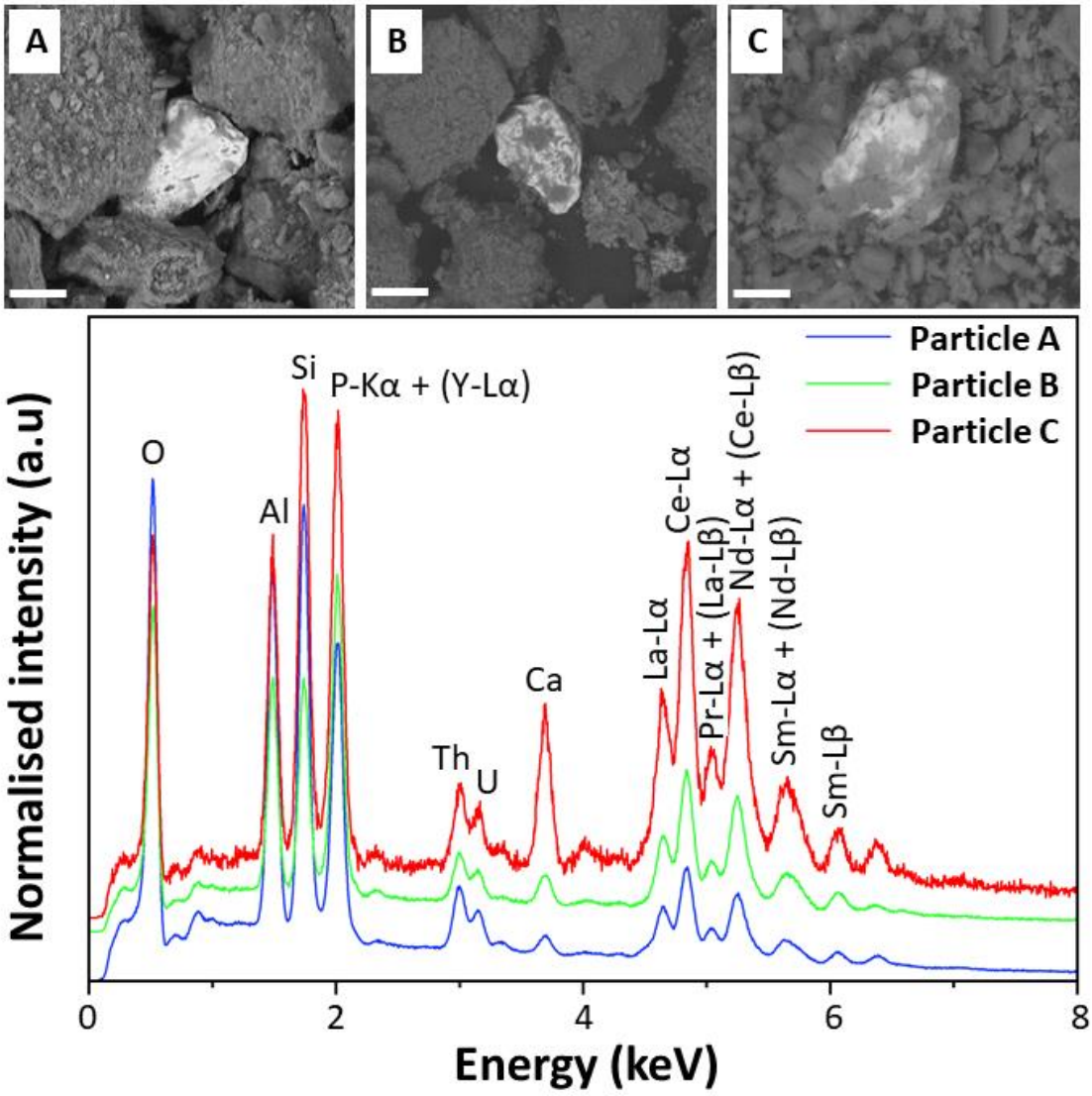

Fig. 3b: (top) Electron microscope images of monazite particles (**A**, **B** and **C**) alongside, (bottom) the associated EDS spectra, with emission peaks identified. (Scale bars = 50 μm).

3.4 μ-XRF

Fig. 4 shows the elemental composition maps of monazite particles **A, B** and **C.** From the results, the monazite particles show a core-shell pattern, with the shell rich in strongly colocalised Ce, La and Nd, and a Th and U rich core. U and Th were both observed to colocalise strongly, however, both poorly with the LREE. The chemical similarities (such as atomic radius) account for this observed colocalisation of the LREE [54]. The core-shell zonation of the actinides and LREE in the monazite particles is characteristic of detrital monazite, formed during magmatic growth or recrystallisation of the monazite particles [55].

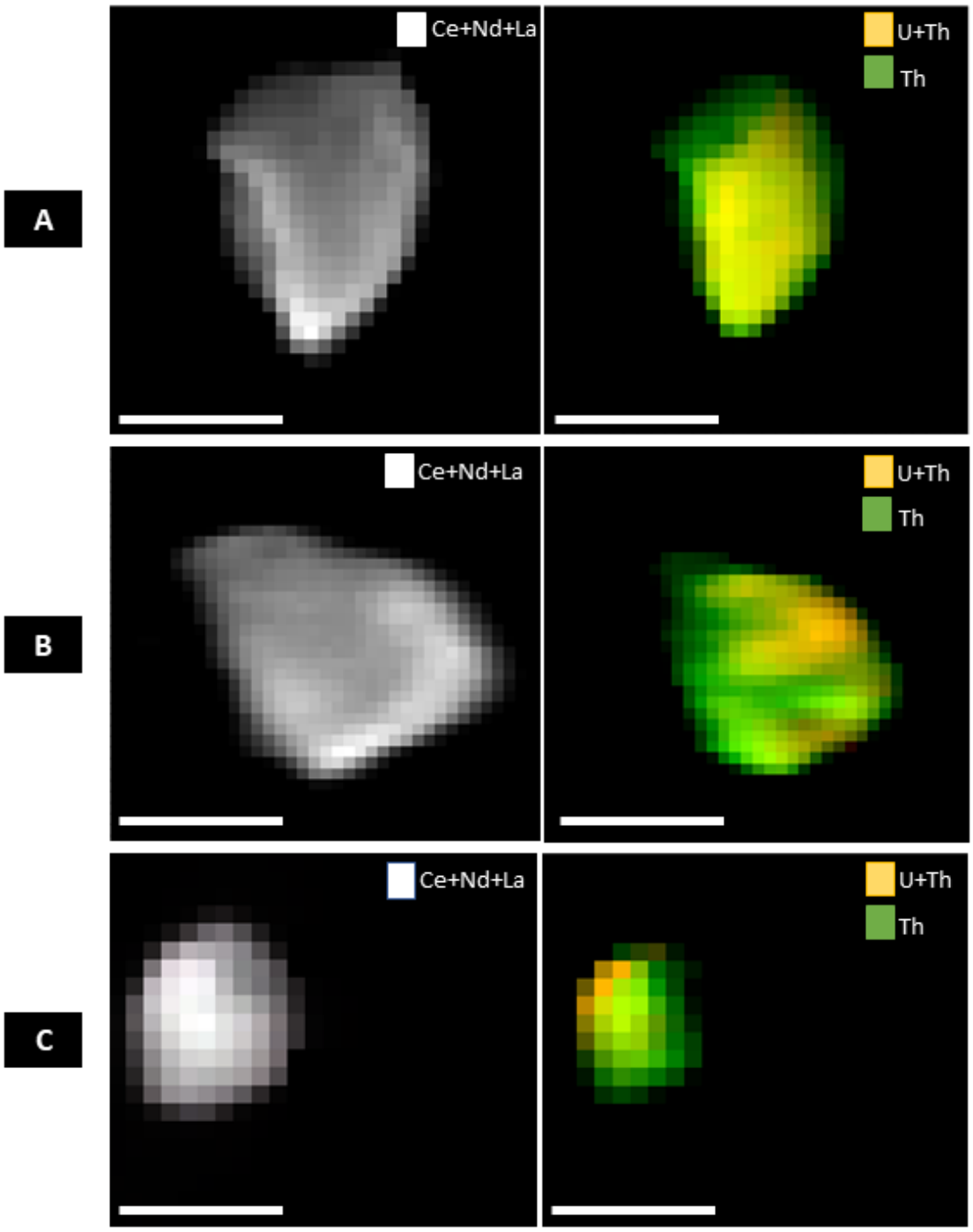

Fig. 4: µ-XRF maps (Ce, Nd, La, U and Th) of monazite particles **A**, **B** and **C,** illustrating the compositional variance of these elements (scale bars = 50 µm).

3.5 µ-XRF tomography

Renderings of the µ-XRF tomography data on monazite particle **A** are shown in Figs. 5, 6 and 7. The results highlight the core-shell distribution of elements within the particle (Fig. 6), with the REE Ce, La and Nd confirmed to be surface bound, surrounding Th and U (Figs. 6 and 7). Both Th and U were

observed to exist as strongly colocalised in the core of the monazite particle, while being simultaneously depleted around its shell [Figs. 6 and 7], confirming the earlier µ-XRF results. Being surface bound, these REE would have the potential to be preferentially leached during an extraction process (compared to U and Th, that are conversely located within the particle centre). This finding is significant in the development of a selective extraction methodology, targeting the strongly colocalised and surface bound REE in fly ash monazite particles. The µ-XRF tomography results have also illustrated that the monazite particle is of high density and is also non-porous; implying that the surface pits (identified by the SEM imaging) do not permeate significantly into the underlying monazite structure.

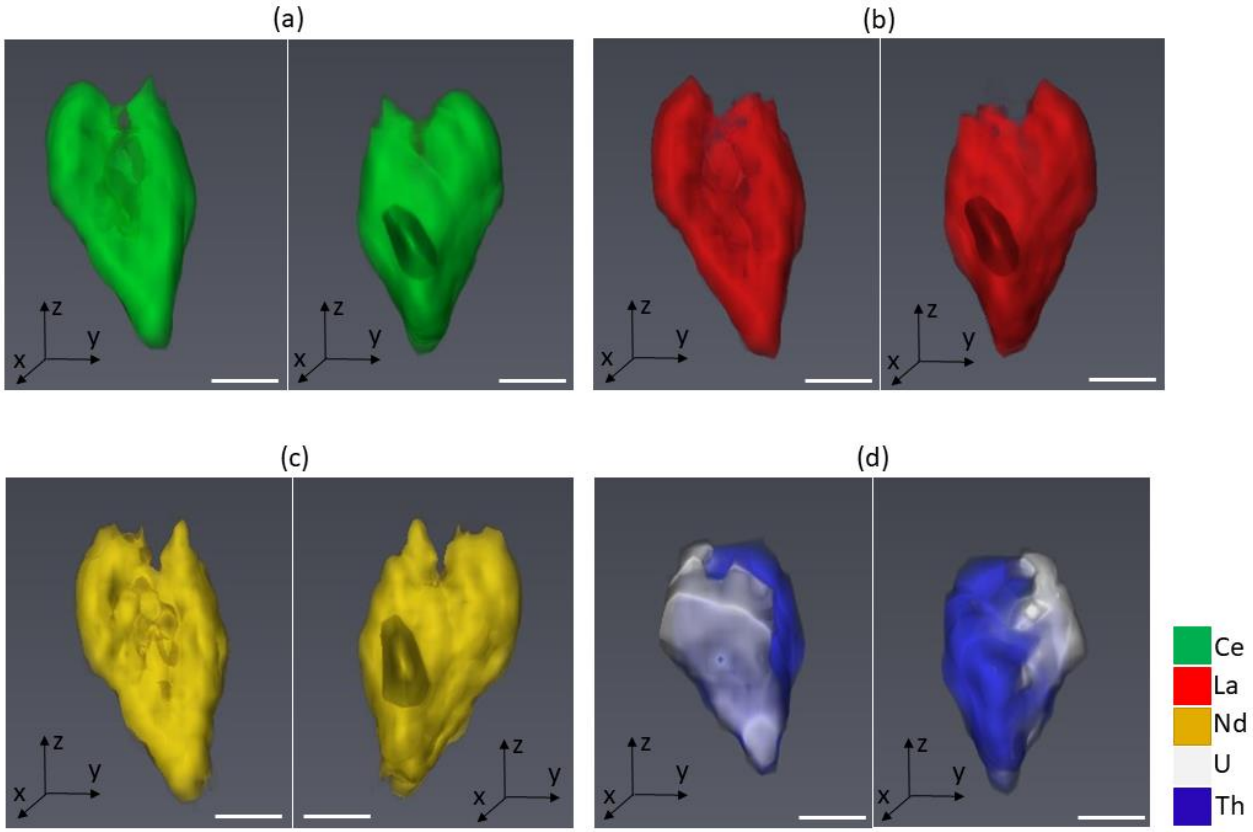

Fig. 5: 3D volumetric rendering (Front and back views) of Ce, La, Nd, U and Th in monazite particle **A.** Scale bars = 25 µm.

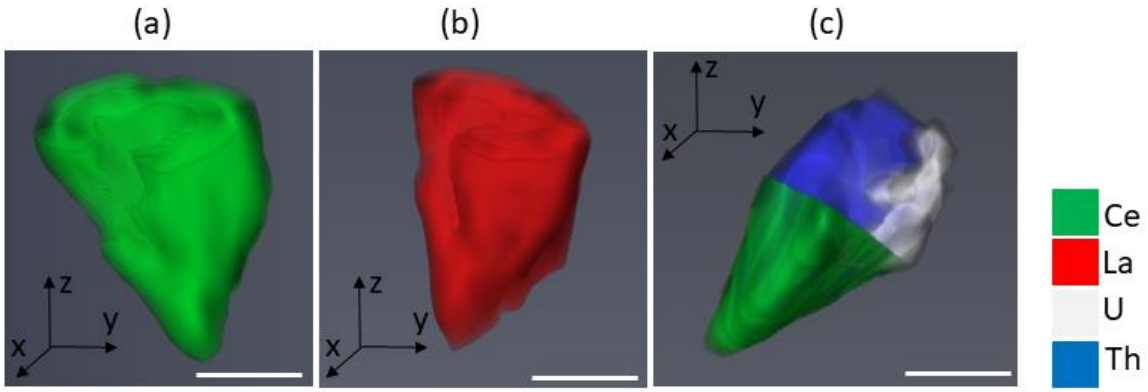

Fig. 6: Cut sections of 3D volumetric renderings of monazite particle **A** showing the core-shell pattern. (a) and (b): hollow interior within Ce and La volumetric renderings. (c): Ce outer shell with U and Th components within the core**.** Scale bars = 25 µm.

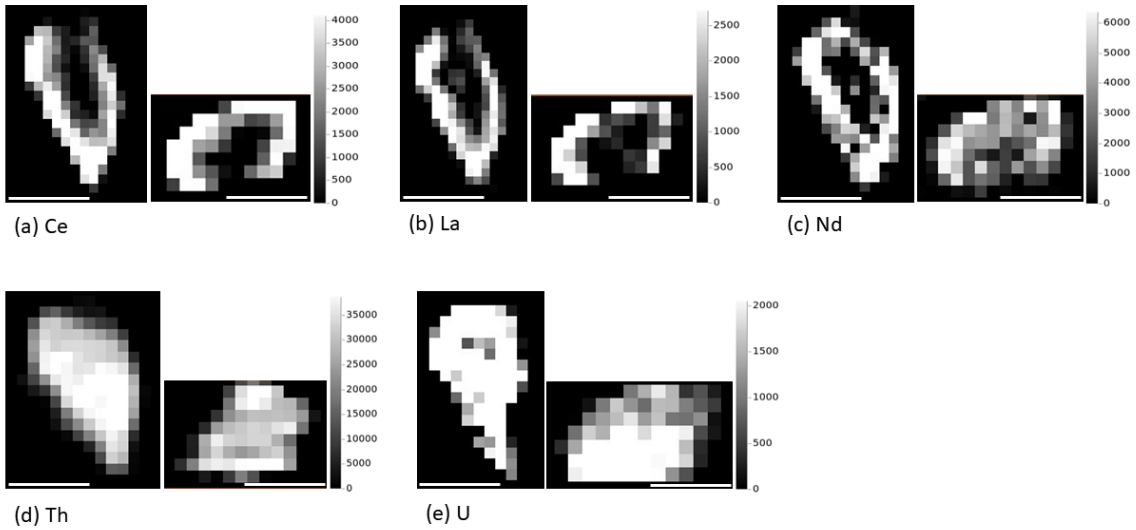

Fig. 7: Greyscale plots in the xy and xz planes (arbitrary units) showing monazite particle **A** with a REE rich rim and a REE depleted core. Scale bars = 25 µm.

3.6 µ-XANES

The µ-XANES spectrum across the Ce, La and Nd L_{III}-edge in monazite particles **A, B** and **C**, alongside their reference standards [57], are shown in Figs. 8a-8c. from Fig. 8a, the Ce (III) reference has a single peak at *P* (5727.5 eV) with the peaks at *Q* (5731 eV) and *R* (5738 eV) representing the Ce (IV) reference. The µ-XANES spectrum of Ce in particle **A** (Fig. 8a) displays two peaks-an intense peak at 5727.5 eV (position *P*), corresponding to Ce (III), and a subtle peak at 5738 eV (position *R*), corresponding to Ce (IV) minor contribution. This invokes a micro-scale oxidation of Ce (transitioning from III to IV) resulting

from the thermal decomposition of the detrital monazite particles, during the high temperature combustion process and illustrates that Ce existed in mixed oxidation states of III and IV. Ce (III) has the tendency to lose an electron to become $4f^0$, and hence form the stable Ce (IV) [54]. LCF using Ce (III) ($CeTiO_3$) and Ce (IV) (CeO_2) references revealed a Ce (III) and Ce (IV) ratio of 80%:20% (Table 2), which affirms a micro scale oxidation due to the high temperature combustion process. These results agree with an earlier work, noting possible processing differences [24].

Both La and Nd in particles **A**, **B** and **C** (Figs. 8b and 8c) were found to exist only in the III oxidation state, with distinct peak at 5485 eV and 6214 eV, respectively. This result coupled with the existence of similarity in the pre- and post-edge features between the particles and reference La and Nd spectra, suggest that the La and Nd chemistry for the particles is unaffected by the high temperature combustion process and resistant to oxidation. The similarity in chemical properties of the REE explains the prevalence of the 3+ oxidation state.

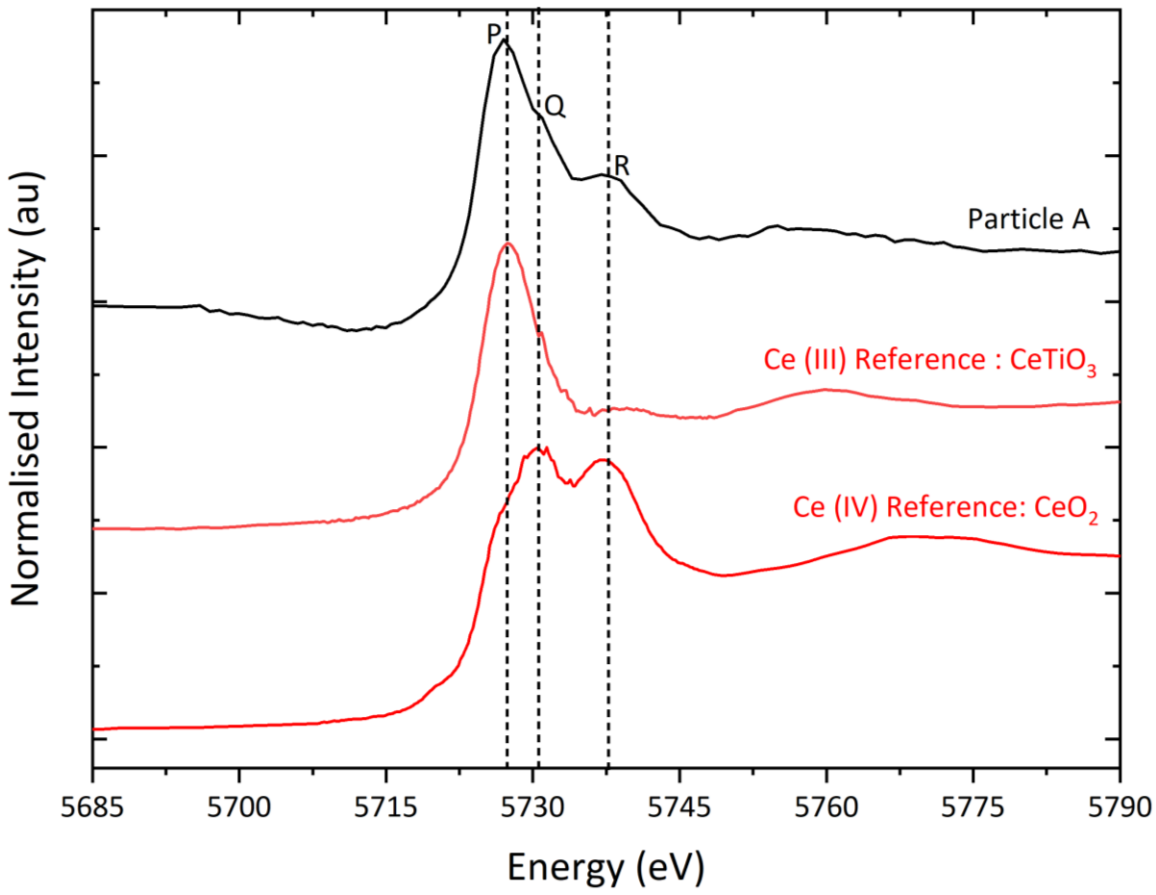

Fig. 8a: XANES spectrum of Ce in monazite particle **A** alongside its references [56]. Point P represents Ce (III) peak, and points Q and R represents Ce (IV) peaks.

Table 2: LCF results of Ce µ-XANES detailing the weight of Ce oxidation states.

	Component	Component weight (in % ± uncertainty)	R-factor[a]
Particle **A**	$CeTiO_3$ (Ce III)	80.2 ± 0.044	0.038
	CeO_2 (Ce IV)	19.8 ± 0.062	
		Sum: 100	

a R-factor defines the goodness of a fit, given as $\frac{sum\,[(data-fit)^2]}{sum\,(data^2)}$. Smaller R- factor represents a better fit.

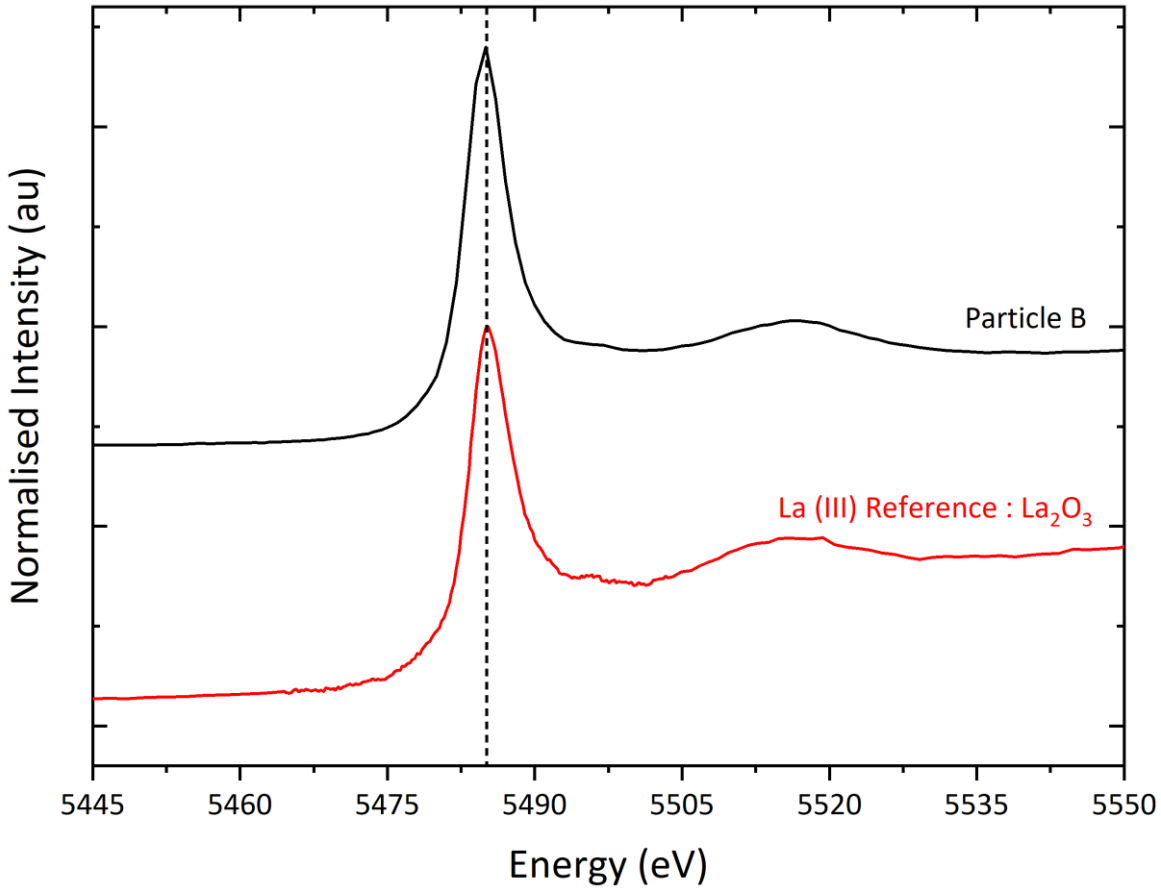

Fig. 8b: XANES spectrum of La in monazite particle **A** alongside its reference [56].

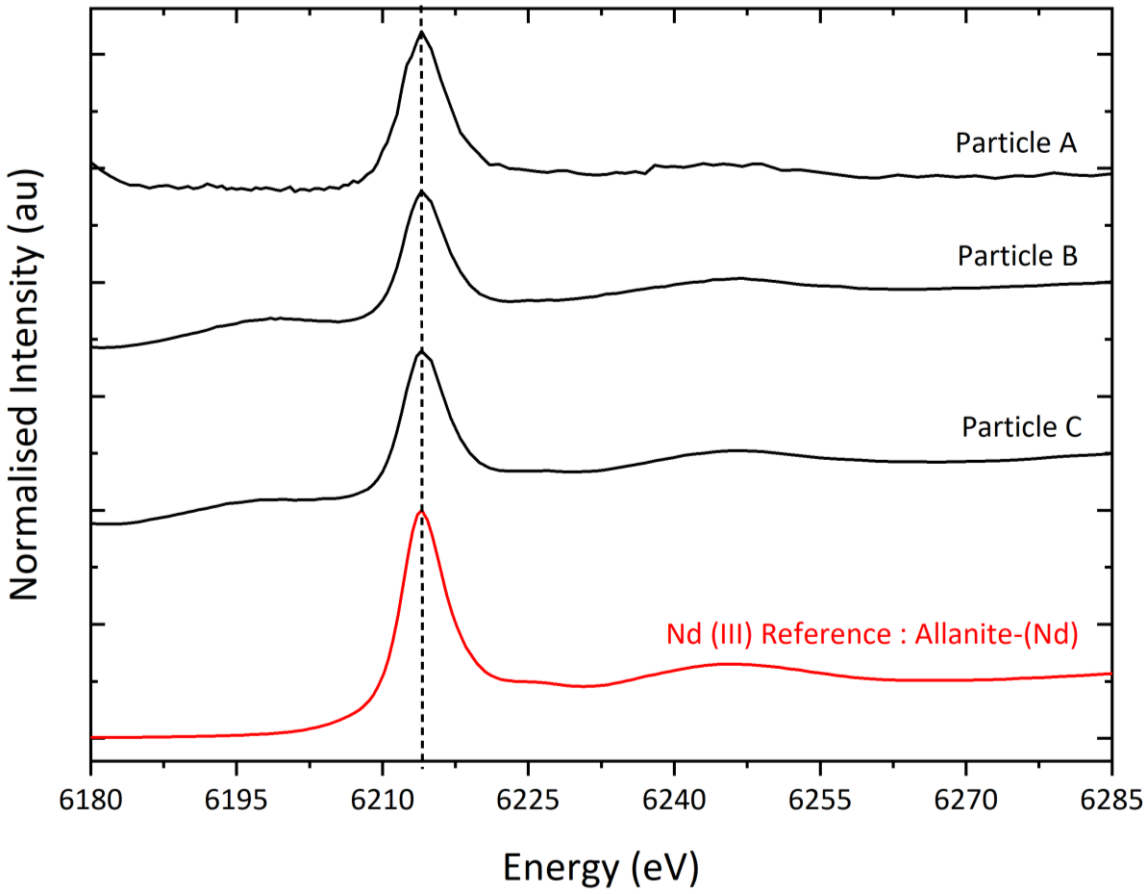

Fig. 8c: XANES spectrum of Nd in monazite particle **A, B** and **C** alongside its reference [56].

3.7 µ-XRD

The 2D and 1D µ-XRD patterns of particles **A**, **B** and **C** (Fig. 9) showed poorly formed diffuse diffraction rings, broad halo and lacking well-defined diffraction peaks, characteristic of amorphous materials. This implies partial or total amorphization/metamictization of the (naturally crystalline) monazite particle due to combined effects of alpha irradiation by uranium and thorium of the particles, combined with the high temperature ashing/combustion process. This radiation and/or high temperature induced structural transformation post combustion is vital in understanding the chemical reactivity, solubility and extractability of the REE from fly ash. Amorphization lowers the hardness of monazite thereby making it more susceptible to chemical attack with increased solubility. Monazite leaching can be done using a less aggressive dilute mineral acid at a lower temperature and in less time, which is more economical and with a higher REE extraction efficiency, than the conventional processes.

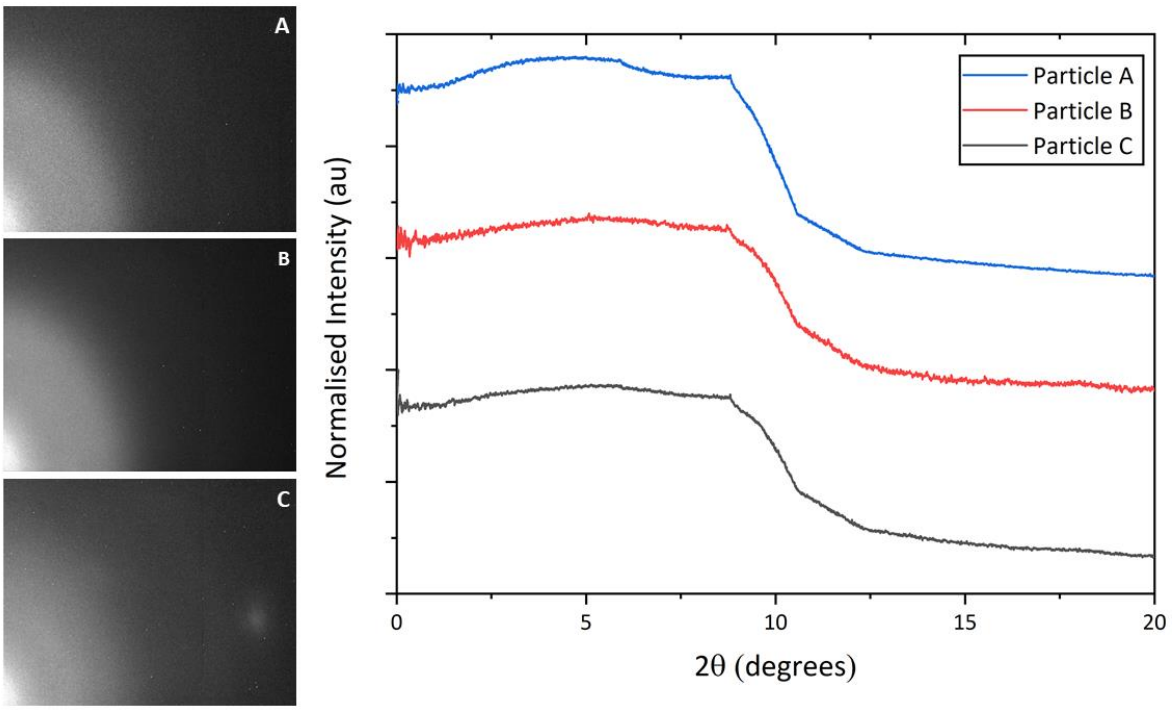

Fig. 9: 2D and 1D µ-XRD patterns of monazite particles **A, B** and **C.**

4. Summary

This work has determined the REE abundance and distribution in Nigerian fly ash. This knowledge is essential to optimise the future REE recovery methods while simultaneously safeguarding the environment from potential rare earth and heavy metal contamination, if released. Furthermore, this study has also demonstrated a new method whereby individual monazite particles are removed from bulk samples using an SEM-mounted micromanipulator (prior to synchrotron radiation analysis), which has been demonstrated as being able to significantly enhance the resolution and quality of the results obtained when compared to conventional 'bulk' characterisation methods.

The average total REE (plus Y and Sc) mass fractions in OMA, OKA and ODA fly ash samples were 623 $mgkg^{-1}$, 442 $mgkg^{-1}$ and 441 $mgkg^{-1}$, respectively. Additionally, analysis determined the existence of dispersed (discrete) rare earth minerals (of detrital origin) with sizes between 10 µm and 70 µm in the fly ash samples, with light REE in the monazite particles strongly colocalised and surface bound – enveloping the actinides in a core-shell pattern. Ce was found to exist in mixed oxidation states (but

predominantly in the (III) oxidation state), with Nd and La being very stable in state III and unaffected by the high temperature combustion process. Both U and Th were observed to be strongly colocalised, were observed to be concentrated in the particle's interior and depleted around the circumference. The monazite particles were metamict/amorphous which is attributed to irradiation and the high coal combustion temperature. To the authors knowledge, such identification of elemental zonation within isolated monazite particles derived from fly ash material represents the first complementary synchrotron radiation μ-XRF and μ-XRF tomography study on coal fly ash. And while based only on an indicative sample set, these initial results are very significant for the optimization and development of rare earth extraction methods and represent a potentially highly valuable source for prized REE from an otherwise pure waste product.

Acknowledgements

The authors wish to thank Diamond Light Source for rapid access to beamline I18 (SP22876) that contributed to the results presented here. We also wish to thank the Commonwealth Scholarship Commission for funding the PhD studentship.

Appendix A. Supplementary data

Supplementary data to this article can be found online at doi: …

Funding

The SEM used in this work to conduct imaging and EDS analysis was purchased following funding by the Engineering and Physical Sciences Research Council (EPSRC), (Reference: EP/K040340/1).

Declarations of interest: none.

References

[1] Xiaoyue Du and Graedel T. E. Global In-Use Stocks of the Rare Earth Elements: A First Estimate. Environ. Sci. Technol., 45 (2011), pp. 4096–4101. dx.doi.org/10.1021/es102836s

[2] BBC. Are rare earth minerals China's trump card in its trade war with the US? https://www.bbc.com/news/amp/world-asia-48366074, 2019 (accessed 30 May 2019).

[3] British Geological Survey (BGS). Rare earth elements. www.MineralsUK.com, 2011 (accessed 18 July 2019).

[4] Asian Metals. Rare earth minerals and classification. http://metalpedia.asianmetal.com, 2019 (accessed 6 July 2019).

[5] Weng, Z. H., Jowitt, S. M., Mudd, G. M., Haque, N. Assessing rare earth element mineral deposit types and links to environmental impacts. Trans. Inst. Min. Metall., Sect. B., 122 (2013), pp. 83−96. DOI 10.1179/1743275813Y.0000000036

[6] Jordens, A., Cheng, Y. P., Waters, K. E. A review of the beneficiation of rare earth element bearing minerals. Miner. Eng., 41 (2013), pp. 97−114. http://dx.doi.org/10.1016/j.mineng.2012.10.017

[7] Wedepohl, K. H. The composition of the continental crust. Geochim. Cosmochim. Acta, 59 (1995), pp. 1217−1232. https://doi.org/10.1016/0016-7037(95)00038-2

[8] Ross K. Taggart, James C. Hower, Gary S. Dwyer, and Heileen Hsu-Kim. Trends in the Rare Earth Element Content of U.S.-Based Coal Combustion Fly Ashes. Environ. Sci. Technol., 50 (2016), pp. 5919−5926. DOI:10.1021/acs.est.6b00085.

[9] Kanazawa, Y.; Kamitani, M. Rare earth minerals and resources in the world. J. Alloys Compd., 408−412 (2006), pp. 1339−1343. http://dx.doi.org/10.1016/j.jallcom.2005.04.033

[10] US senate committee on energy & natural resources. Manchin, Capito & Murkowski Reintroduce Rare Earth Element Advanced Coal Technologies Act. www.energy.senate.gov, 2019 (accessed 6 May 2019).

[11] Mardon, S. M.; Hower, J. C. Impact of coal properties on coal combustion by-product quality: examples from a Kentucky power plant. Int. J. Coal Geol., 59 (2004), pp. 153−169. http://dx.doi.org/10.1016/S0166-5162(04)00033-3

[12] Hower, J. C.; Ruppert, L. F.; Eble, C. F. Lanthanide, yttrium, and zirconium anomalies in the Fire Clay coal bed, Eastern Kentucky. Int. J. Coal Geol., 39 (1999), pp. 141−153. https://doi.org/10.1016/S0166-5162(98)00043-3

[13] Seredin, V. V.; Dai, S. Coal deposits as potential alternative sources for lanthanides and yttrium. Int. J. Coal Geol., 94 (2012), pp. 67−93. DOI: 10.1016/j.coal.2011.11.001

[14] Seredin, V. V. Rare earth element-bearing coals from the Russian Far East deposits. Int. J. Coal Geol., 30 (1996), pp. 101−129. https://doi.org/10.1016/0166-5162(95)00039-9

[15] National Energy Technology Laboratory, U.S. Department of Energy. Characterization of Rare Earth Element Minerals in Coal Utilization By-products.

https://edx.netl.doe.gov/dataset/characterization-of-rare-earth-element-minerals-in-coal-utilization-byproducts, 2017 (accessed 8 May 2019).

[16] National Energy Technology Laboratory, U.S. Department of Energy. Rare Earth Element, 2019 project portfolio.

https://netl.doe.gov/sites/default/files/2019-04/2019-REE-Project-Portfolio.pdf, 2019 (accessed 2 July 2019).

[17] Hood M.M., Targgart R.K., Smith R.C., Hsu-Kim H., Henke K.R., Graham U., Groppo J.G., Unrine J.M., Hower J.C. Rare earth element distribution in fly ash derived from the Fire Clay coal, Kentucky. Coal Combust. Gasificat. Products, 9 (2017), pp. 22-33. doi: 10.4177/CCGP-D-17-00002.1

[18] Hower J.C., Eble C.F., Dai S.,Belkin H.E. Distribution of rare earth elements in eastern Kentucky coals: indicators of multiple modes of enrichment? Int. J. Coal Geol., 160-161 (2016), pp. 73-81. DOI: 10.1016/j.coal.2016.04.009

[19] Montross S.,Circe A.V.,Falcon A., Poston J., Mark M. Characterization of rare earth element minerals in coal utilization by-products and associated clay deposits from Appalachian Basin coal resources. 34th International Pittsburgh Coal Conference Pittsburgh, PA. (2017).

[20] Newville M. Fundamentals of XAFS. Consortium for Advanced Radiation Sources, University of Chicago, Chicago, IL. (2004).

[21] Smith J.V., Rivers M.L., Potts P.J., Bowles J.F.W., Reed S.J.B., Cave M.R. Synchrotron X-ray microanalysis, Microprobe Techniques in the Earth Sciences, Springer US, Boston, MA, (1995), pp. 163-233

[22] Takahashi Y., Shimizu H., Usui A., Kagi H., Nomura M. Direct observation of tetravalent cerium in ferromanganese nodules and crusts by X-ray-absorption near-edge structure (XANES). Geochim. Cosmochim. Acta, 64 (2000), pp. 2929-2935

[23] Takahashi Y., Sakami H., Nomura M. Determination of the oxidation state of cerium in rocks by Ce LIII-edge X-ray absorption near-edge structure spectroscopy. Anal. Chim. Acta, 468 (2002), pp. 345-354. https://doi.org/10.1016/S0016-7037(00)00403-8

[24] Mengling Y. Stuckman, Christina L. Lopano, Evan J.Granite. Distribution and speciation of rare earth elements in coal combustion by-products via synchrotron microscopy and spectroscopy. International Journal of Coal Geology, 195 (2018), pp. 125-138. https://doi.org/10.1016/j.coal.2018.06.001

[25] Pan Liu, Rixiang Huang, Yaunzhi Tang. Comprehensive understandings of rare earth element (REE) speciation in coal fly ashes and implication for REE extractability. Environmental science and technology, 53 (2019), pp. 5369-5377. DOI: 10.1021/acs.est.9b00005

[26] Thibault Cheisson and Eric J. Schelter. Rare earth elements: Mendeleev's bane, modern marvels. Science 363 (2019), pp. 489–493. DOI: 10.1126/science.aau7628

[27] Ilemona C. Okeme, Thomas B. Scott, Peter G. Martin, Yukihiko Satou, Theophilus I. Ojonimi, Moromoke O. Olaluwoye. Assessment of the mode of occurrence and radiological impact of radionuclides in Nigerian coal and resultant post-combustion coal ash using scanning electron microscopy and gamma-ray spectroscopy. Minerals, 10 (2020), https://doi.org/10.3390/min10030241.

[28] Onoduku, Usman Shehu. Geochemical Evaluation of Okaba (Odagbo) Coal Deposit, Anambra Basin, Nigeria. RJSITM, 03 (2014), ISSN: 2251-1563

[29] Ministry of Solid Minerals Development, Federal Republic of Nigeria. Feasibility Study: Nigerian Coal Resource Development. https://electricityinnigeria.com/, 2006 (accessed 18 March 2019).

[30] Afu D.J., Ifeola E.O. and Adesida P.A. Omelewu coal characterisation for powering power plant at Dangote cement factory, Obajana, Kogi state, Nigeria. American journal of engineering research, 7 (2018), pp. 143-152. e-ISSN: 2320-0847.

[31] Mohammed U. Garba, Umaru Musa, Priscilla E. Azare, Kariim Ishaq, Usman S. Onoduku, Yahaya S. Mohammad. Characterisation and ash chemistry of selected Nigerian coals for solid fuel combustion. Petoleum and coal, 58 (2016), pp. 646-654. ISSN: 1337-7027.

[32] Chukwu M., Folayan C.O., Pam G.Y., Obada D.O. Characterisation of some Nigerian coals for power generation. Journal of combustion, 2016. http://dx.doi.org/10.1155/2016/9728278.

[33] energy mix report. ETA-ZUMA launches coal briquette production plant-Kogi state. www.energymixreport.com/eta-zuma-launches-coal-briquette-production-plant-kogi/, 2018 (accessed 7 June 2018).

[34] Franklin Alli. Cement Manufacturers Cut Power Cost with Investments in Coal. www.vanguardngr.com/2017/11/cement-manufacturers-cut-power-cost-coal-investments/, 2017 (accessed 8 June 2018).

[35] The Presidency, Federal Republic of Nigeria. National energy policy. www.energy.gov.ng/, 2003 (accessed 12 July 2019).

[36] Pulverised coal combustion (PCC). https://www.iea-coal.org/pulverised-coal-combustion-pcc/. (Accessed 4 January 2018).

[37] Carl-Dieter Garbe-Schönberg. Simultaneous determination of thirty-seven trace elements in twenty-eight international standards by ICP-MS. Geostandards newsletter, 17 (1993) pp. 81-97.

[38] Kleindiek Nanotechnik GmbH, 'MM3A-EM Micromanipulator product brochure', tech.rep., Reutlingen, Germany.

[39] Martin P.G., Griffiths I., Jones C.P., Stitt C.A., Davies-Milner M., Mosselmans J.F.W., Yamashiki Y., Richards D.A., Scott T.B. In-situ removal and characterisation of uranium-containing particles from sediments surrounding the Fukushima Daiichi Nuclear Power Plant. Spectrochimica Acta Part B: Atomic Spectroscopy, 117 (2016), pp. 1-7. https://doi.org/10.1016/j.sab.2015.12.010.

[40] Kleindiek Nanotechnik GmbH, 'SEMGlu product brochure '.

[41] Mosselmans J.F.W., Quinn P.D., Dent A.J. Cavill S.A., Moreno S.D., Peach A., Leicester P.J., Keylock S.J., Atkinson K.D., Rosell J.R., Gregory S.R. I18-The microfocus spectroscopy beamline at the Diamond Light Source. J. Synchrotron Radiat., 16 (2009), pp. 818-824, 10.1107/S0909049509032282.

[42] Basham, M., Filik, J., Wharmby, M.T., Chang, P.C.Y., El Kassaby, B., Gerring, M., Aishima, J.,

Levik, K., Pulford, B.C.A., Sikharulidze, I. et al. Data Analysis WorkbeNch (DAWN). J. Synchrotron Rad. 22 (2015), pp. 853-858. doi:10.1107/S1600577515002283

[43] Thermo Fisher Scientific. Amira-Avizo Software: 3D visualization and analysis software. (2019).

[44] Ravel B. and Newville M. ATHENA, ARTEMIS, HEPHAESTUS: data analysis for X-ray absorption spectroscopy using IFEFFIT. J. of synch. Rad., 12 (2005), pp. 537-541. 10.1107/S0909049505012719

[45] ASTM C618-19: Standard specification for coal fly ash and raw or calcined natural pozzolan for use in concrete. https://compass.astm.org/. (Accessed 7 March 2018).

[46] Ross K. Taggart, James C. Hower, Gary S. Dwyer, Heileen Hsu-Kim. Trends in the rare earth element content of U.S-based coal combustion fly ashes. Environ. Sci. Technol., 50 (2016), pp. 5919-26. Doi: 10.1021/acs.est.6b00085

[47] Zhen Wang, Shifeng Dai, Jianhua Zou, David French, Ian T. Graham. Rare earth elements and yttrium in coal ash from the Luzhou power plant in Sichuan, Southwest China: concentration, characterisation and optimised extraction, 203 (2019), pp. 1-14 https://doi.org/10.1016/j.coal.2019.01.001.

[48] S.F. Dai, L. Zhao, J.C. Hower, M.N. Johnston, W.J. Song, P.P. Wang, S.F. Zhang. Petrology, mineralogy, and chemistry of size-fractioned fly ash from the Jungar power plant, Inner Mongolia, China, with emphasis on the distribution of rare earth elements**.** Energy Fuel, 28 (2014), pp. 1502-1514. https://doi.org/10.1021/ef402184t

[49] Modal S., Ghar A., Satpati A.K., Sinharoy P., Singh D.K., Sharma J.N., Sreenivas T., Kain V. Recovery of rare earth elements from coal fly ash using TEHDGA impregnated resin. Hydrometallurgy, 185 (2019), pp. 93-101. https://doi.org/10.1016/j.hydromet.2019.02.005

[50] Mardon, S. M.; Hower, J. C. Impact of coal properties on coal combustion by-product quality: examples from a Kentucky power plant Int. J. Coal Geol., 59 (2004), pp. 153–169. DOI:10.1016/j.coal.2004.01.004

[51] J.C. Hower, J.G. Groppo, P. Joshi, S. Dai, D.P. Moecher, M. Johnston. Location of cerium in coal combustion fly ashes: implications for recovery of lanthanides Coal Combust. Gasificat. Prod. (2013b), pp. 73-78

[52] R.K. Taggart, J.C. Hower, G.S. Dwyer, H. Hsu-KimTrends in the rare earth element content of U.S.-based coal combustion fly ashes. Environ. Sci. Technol., 50 (2016), pp. 5919-5926. https://doi.org/10.1021/acs.est.6b00085

[53] Pingitore Nicholas, Clague Juan, Gorski Daniel. Round top mountain rhyolite (Texas, usa), a massive, unique Y-bearing-fluorite-hosted heavy rare earth element deposit. Journal of rare earths, 32 (2014), https:///doi.org/10.1016/S1002-0721(14)60037-5.

[54] Cotton S. Lanthanide and actinide chemistry. Chichester, England: John Wiley and Sons; 2006.

[55] Elizabeth J. Catlos. Generalisations about monazite: implications for geochronologic studies. American mineralogist, 98 (2013), pp. 819-832

[56] International X-ray Absorption Society, 'XAFS Materials Database'. http://ixs.iit.edu/database/data/Farrel_Lytle_data/RAW/index.html. (Accessed 6 March 2019).

Ilemona Okeme and **Thomas Scott**: Conceptualization, Methodology. **Ilemona Okeme**, **Peter Martin**, **Konstantin Ignatyev**, **Christopher Jones** and **Richard Crane**: Software, validation, Data curation, Investigation, Formal analysis, Visualisation, Writing- Original draft preparation. **Ilemona Okeme** and **Theophilus Ojonimi**: Resources. **Ilemona Okeme** and **Peter Martin**: Writing- Reviewing and Editing.